The Astrophysical Journal, 851:96 (12pp), 2017 December 20 https://doi.org/10.3847/1538-4357/aa9ce6

Upward and Downward Catastrophes of Coronal Magnetic Flux Ropes in Quadrupolar Magnetic Fields

Quanhao Zhang[1], Yuming Wang[1,2], Youqiu Hu[1], Rui Liu[1,3], Kai Liu[1,4], and Jiajia Liu[1,4]
[1] CAS Key Laboratory of Geospace Environment, Department of Geophysics and Planetary Sciences, University of Science and Technology of China, Hefei, Anhui 230026, China; zhangqh@mail.ustc.edu.cn
[2] Synergetic Innovation Center of Quantum Information and Quantum Physics, University of Science and Technology of China, Hefei, Anhui 230026, China
[3] Collaborative Innovation Center of Astronautical Science and Technology, Hefei, Anhui 230026, China
[4] Mengcheng National Geophysical Observatory, School of Earth and Space Sciences, University of Science and Technology of China, Hefei, Anhui 230026, China
Received 2017 February 24; revised 2017 October 27; accepted 2017 November 21; published 2017 December 15

Abstract

Coronal magnetic flux ropes are closely related to large-scale solar activities. Using a 2.5-dimensional time-dependent ideal magnetohydrodynamic model in Cartesian coordinates, we carry out numerical simulations to investigate the evolution of a magnetic system consisting of a flux rope embedded in a fully closed quadrupolar magnetic field with different photospheric flux distributions. It is found that when the photospheric flux is not concentrated too much toward the polarity inversion line and the constraint exerted by the background field is not too weak, the equilibrium states of the system are divided into two branches: the rope sticks to the photosphere for the lower branch and levitates in the corona for the upper branch. These two branches are connected by an upward catastrophe (from the lower branch to the upper) and a downward catastrophe (from the upper branch to the lower). Our simulations reveal that there exist both upward and downward catastrophes in quadrupolar fields, which may be either force-free or non-force-free. The existence and the properties of these two catastrophes are influenced by the photospheric flux distribution, and a downward catastrophe is always paired with an upward catastrophe. Comparing the decay indices in catastrophic and noncatastrophic cases, we infer that torus unstable may be a necessary but not sufficient condition for a catastrophic system.

Key words: Sun: coronal mass ejections – Sun: filaments, prominences – Sun: flares – Sun: magnetic fields

1. Introduction

It is well known that large-scale solar eruptive activities, including prominence/filament eruptions, flares, and coronal mass ejections, are closely related to solar magnetic flux ropes (e.g., Low 1996; Chen 2011; Shibata & Magara 2011; Wang et al. 2015). In order to understand the physical processes of solar eruptive activities, various theoretical models have been proposed to describe the eruption of solar magnetic flux ropes, invoking distinctive physical mechanisms, e.g., magnetic reconnections (Antiochos et al. 1999; Chen & Shibata 2000; Moore et al. 2001), magnetohydrodynamic (MHD) instabilities (Amari et al. 2000; Kliem & Török 2006; Liu et al. 2007), and catastrophe. The catastrophe of flux rope systems was first proposed by Van Tend & Kuperus (1978), who concluded that if the current in a filament exceeds a critical value, then a catastrophic loss of equilibrium occurs in the magnetic system. Both analytical and numerical analyses have been made to investigate the catastrophic behaviors of solar magnetic flux ropes and leading to a common conclusion that catastrophe could be responsible for flux rope eruptions (Forbes 1990; Priest & Forbes 1990; Forbes & Isenberg 1991; Isenberg et al. 1993; Forbes & Priest 1995; Lin & Forbes 2000; Lin & van Ballegooijen 2002; Zhang & Wang 2007; Su et al. 2011). These studies focus on the equilibrium manifold in parameter space, i.e., the evolution of the equilibrium states of the system as a function of a certain control parameter characterizing the physical properties of the system. In analytical analyses, the equilibrium manifold is obtained by solving the force balance equation, whereas in numerical simulations it is obtained by calculating the different equilibrium states with different values of the control parameter. The critical value of the control parameter at which catastrophe occurs is called catastrophic point, which usually appears as an end or nose point of the equilibrium manifold (Kliem et al. 2014; also see Figure 1). Magnetic free energy is always released and converted to kinetic and thermal energy during catastrophe (Chen et al. 2007a), via both magnetic reconnection and the work done by Lorentz force (Chen et al. 2007b; Zhang et al. 2016). Previous studies also demonstrated that catastrophe and instability are intimately related in the evolution of magnetic flux rope systems (Démoulin & Aulanier 2010; Kliem et al. 2014; Longcope & Forbes 2014).

Cartesian coordinates are widely used to investigate active region activities. Using a 2.5-dimensional ideal MHD model in Cartesian coordinates, Hu (2001) found that the equilibrium states of the magnetic system consisting of a flux rope embedded in a partially open bipolar background field are divided into upper and lower branches, and there exists an upward catastrophe from the lower branch to the upper branch. By simulating the evolution of a similar system under different photospheric magnetic conditions, Zhang et al. (2017) found that the upward catastrophic behavior of the magnetic system is influenced by the photospheric magnetic condition: namely, the transition from the equilibrium state with the flux rope sticking to the photosphere (hereafter, the "sticky" state) to that with the flux rope levitating in the corona (hereafter, the "levitating" state) varies with the photospheric magnetic flux distribution. When the photospheric flux is not concentrated too much toward the polarity inversion line (PIL) and the source regions of the bipolar field are not too weak, the sticky and levitating states are separated and correspond to the lower and upper branches, respectively. Otherwise, the transition between the sticky and the levitating states is continuous, implying that the system is noncatastrophic. Note that previous studies

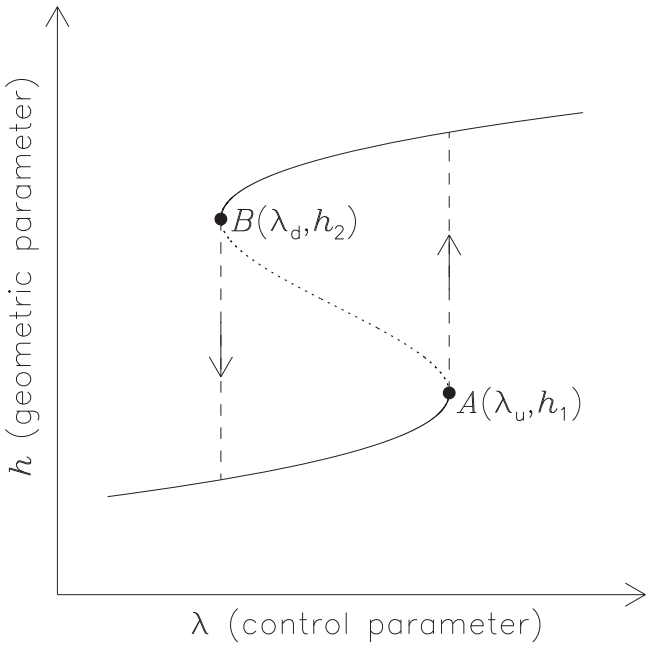

Figure 1. Schematic cartoon of the equilibrium manifold with both upward and downward catastrophe. λ is the control parameter and h is the geometric parameter. Upward and downward catastrophes occurs at the nose points A and B, respectively, and λ_u and λ_d are the corresponding catastrophic points.

demonstrated that there are two type of flux rope topologies (e.g., Green & Kliem 2009; Savcheva & van Ballegooijen 2009): the flux rope with its underside rooted in the dense lower atmosphere is called a bald-patch separatrix surface (BPSS) configuration (Titov et al. 1993; Titov & Démoulin 1999; Green et al. 2011), and the flux rope levitating in the corona with a magnetic X-type structure beneath is called a hyperbolic flux tube (HFT) configuration (Titov et al. 2002). These two types of configurations and the transition between them have been observed in many studies based on nonlinear force-free field (NLFFF) extrapolations (e.g., Zhao et al. 2014; Savcheva et al. 2015, 2016; Janvier et al. 2016). Comparing with the sticky state and the levitating state, we may infer that the sticky state is consistent with BPSS configurations and the levitating state, in which the flux rope is levitating in the corona with a current sheet below the rope, corresponds to the configuration after the X-type structure in HFT has evolved into a current sheet.

Recently, by expanding the 2.5-dimensional ideal MHD model used in Hu (2001) to force-free approximations, Zhang et al. (2016) found that apart from the well-known upward catastrophe there also exists a downward catastrophe from the upper branch to the lower branch in a partially open bipolar background field. Just like what happens during upward catastrophe, magnetic energy is also released during downward catastrophe, indicating that downward catastrophe may be a mechanism for non-eruptive but energetic activities (e.g., confined flares). Figure 1 is a schematic cartoon of the equilibrium manifold consisting of both upward and downward catastrophes. Here λ is the control parameter and h is the geometric parameter describing the evolution of the equilibrium states (e.g., the height of the rope axis). There are two nose points: A and B, at which upward and downward catastrophe occur, respectively. Obviously, the ill-behaviors of the upward and downward catastrophes result from the fact that the equilibrium manifold is multivalued within the upward (λ_u) and downward (λ_d) catastrophic points.

All the previous numerical simulations about upward and downward catastrophes using the 2.5-dimensional ideal MHD model in Cartesian coordinates are made to investigate the magnetic system in bipolar background fields. Since the magnetic configurations in strong active regions are usually very complex (e.g., Schrijver et al. 2011; Sun et al. 2012; van Driel-Gesztelyi & Green 2015), a quadrupolar background field should be more suitable for analyses of large-scale activities in an active region. In this paper, we simulate the evolution of a magnetic system consisting of a flux rope in a fully closed quadrupolar background field to investigate whether upward and downward catastrophes also exist in quadrupolar fields. Moreover, since only the photospheric magnetic conditions can be observed currently, to reveal the influence of the photospheric conditions on catastrophes could shed light on the physical processes of different solar activities. As mentioned above, previous studies have found that the existence and properties of upward catastrophe are affected by photospheric flux distribution. Thus another intention of this paper is to investigate the influence of photospheric magnetic conditions on downward catastrophe. The sections are arranged as follows: the simulation model in the quadrupolar field is introduced in Section 2, the evolutions of the magnetic system with different photospheric magnetic conditions under force-free and non-force-free conditions are demonstrated in Section 3, and the relationship between catastrophe and torus instability is investigated in Section 4. Finally, a discussion is given in Section 5.

2. Basic Equations and Simulating Procedures

As mentioned in Section 1, a Cartesian coordinate system is used here. A magnetic flux function ψ is introduced to denote the magnetic field as follows:

$$\boldsymbol{B} = \nabla \times (\psi \hat{\boldsymbol{z}}) + B_z \hat{\boldsymbol{z}}. \tag{1}$$

Neglecting the radiation and heat conduction in the energy equation, the 2.5-dimensional MHD equations can be written in the nondimensional form as

$$\frac{\partial \rho}{\partial t} + \nabla \cdot (\rho \boldsymbol{v}) = 0, \tag{2}$$

$$\frac{\partial \boldsymbol{v}}{\partial t} + \boldsymbol{v} \cdot \nabla \boldsymbol{v} + \nabla T + \frac{T}{\rho}\nabla \rho + \frac{2}{\rho \beta_0} \times (\triangle \psi \nabla \psi + B_z \nabla B_z + \nabla \psi \times \nabla B_z) + g\hat{\boldsymbol{y}} = 0, \tag{3}$$

$$\frac{\partial \psi}{\partial t} + \boldsymbol{v} \cdot \nabla \psi = 0, \tag{4}$$

$$\frac{\partial B_z}{\partial t} + \nabla \cdot (B_z \boldsymbol{v}) + (\nabla \psi \times \nabla v_z) \cdot \hat{\boldsymbol{z}} = 0, \tag{5}$$

and

$$\frac{\partial T}{\partial t} + \boldsymbol{v} \cdot \nabla T + (\gamma - 1) T \nabla \cdot \boldsymbol{v} = 0, \tag{6}$$

where ρ, $\boldsymbol{v}$, T, ψ denote the density, velocity, temperature, and magnetic flux function, respectively; the subscript z denotes the $z-$ component of the parameters, which are parallel to the axis of the flux rope; $\beta_0 = 2\mu_0 \rho_0 R T_0 L_0^2 / \psi_0^2 = 0.1$ is the characteristic ratio of the gas pressure to the magnetic pressure, where μ_0

and R are the vacuum magnetic permeability and the gas constant, respectively; $\rho_0 = 3.34 \times 10^{-16}$ g cm^{-3}, $T_0 = 10^6$ K, $L_0 = 10^9$ cm, and $\psi_0 = 3.73 \times 10^9$ Mx cm^{-1} are the characteristic values of density, temperature, length, and magnetic flux function, respectively; and g is the normalized gravity. The initial corona is static and isothermal with

$$T_c \equiv T(0, x, y) = 1 \times 10^6 \text{ K},$$
$$\rho_c \equiv \rho(0, x, y) = \rho_0 e^{-gy}. \quad (7)$$

In this paper, we study the evolution of the magnetic system under both force-free and non-force-free conditions. Force-free equilibrium solutions are obtained by a relaxation method: reset the temperature and density in the computational domain to their initial values so that the pressure gradient force is always balanced everywhere by the gravitational force (Hu 2004).

The background field is a fully closed quadrupolar field, which is assumed to be symmetrical relative to the y-axis. The lower boundary $y = 0$ corresponds to the photosphere. There are two pairs of positive and negative magnetic surface charges located at the photosphere. For the inner pair, which is closer to the PIL, the positive charge is located at $y = 0$ within $-b < x < -a$ and the negative one within $a < x < b$. For the outer pair, the positive and negative charges are located at $y = 0$ within $c < x < d$ and $-d < x < -c$, respectively ($a < b < c < d$). The ratio of the charge density of the inner two charges to that of the outer ones is σ. By a complex variable method, the background magnetic field can be cast in a complex variable form:

$$f(\omega) \equiv B_x - iB_y = \ln\left(\frac{\omega^2 - c^2}{\omega^2 - d^2}\right) - \sigma \ln\left(\frac{\omega^2 - a^2}{\omega^2 - b^2}\right)$$
$$= \ln\left[\frac{(\omega^2 - c^2)(\omega^2 - b^2)^\sigma}{(\omega^2 - d^2)(\omega^2 - a^2)^\sigma}\right], \quad (8)$$

where $\omega = x + iy$. The magnetic flux function is then calculated by

$$\psi(x, y) = \text{Im}\left\{\int f(\omega) d\omega\right\} \quad (9)$$

and the flux function at the photosphere can be derived as

$$\psi_b = \psi(x, 0) = \begin{cases} 0, & x \leqslant -d \\ \pi(x + d), & -d < x \leqslant -c \\ \pi w, & -c < x \leqslant -b \\ \pi w - \sigma\pi(x + b), & -b < x \leqslant -a \\ (1 - \sigma)\pi w, & -a < x \leqslant a \\ \pi w + \sigma\pi(x - b), & a < x \leqslant b \\ \pi w, & b < x \leqslant c \\ \pi(d - x), & c < x \leqslant d \\ 0, & x > d, \end{cases} \quad (10)$$

where $w = b - a = d - c$ is the width of the charges. Here a, b, c, d, and σ characterize the photospheric magnetic flux distribution. With different values of (a, b, c, d, σ), we obtain different background magnetic configurations.

With the initial and boundary conditions, Equations (2)–(6) are solved by the multistep implicit scheme (Hu 1989) to obtain equilibrium solutions of the magnetic system. The computational domain is taken to be $0 \leqslant x \leqslant 100$ Mm, $0 \leqslant y \leqslant 300$ Mm; a symmetric condition is used for the left side of the domain ($x = 0$). During the simulation, potential field conditions are used at the top ($y = 300$ Mm) and right ($x = 300$ Mm) boundaries, and the flux function at the lower boundary ($y = 0$) is fixed at ψ_b.

Starting from a background magnetic configuration with given values of (a, b, c, d, σ), following Hu & Liu (2000) and Hu (2001), we let a flux rope emerge from the central region of the base and then the flux rope sticks to the photosphere, resulting in a magnetic system consisting of a flux rope embedded in a fully closed quadrupolar field, which is the initial state for the given group of (a, b, c, d, σ). The magnetic properties of the flux rope are characterized by the axial magnetic flux passing through the cross-section of the flux rope, Φ_z, and the poloidal magnetic flux of the rope of per unit length along z-direction, Φ_p. Note that Φ_p is simply the difference in ψ between the axis and the outer boundary of the flux rope, negative for the present case with field lines rotating clockwise in the rope. Here we select Φ_z as the control parameter. In our simulation we adjust the values of Φ_z with a fixed Φ_p to calculate different equilibrium solutions of the system; i.e., we analyze the equilibrium manifold as a function of Φ_z, as described by the geometric parameters of the flux rope, including the height of the rope axis, H, and the length of the current sheet below the flux rope, L_c. For the sticky state L_c equals 0, and for the levitating state there is a current sheet below the flux rope so that L_c is finite. For background configurations with different values of (a, b, c, d, σ), similar procedures are repeated so that we obtain the equilibrium manifolds of the flux rope system under different photospheric flux distributions (see Section 3).

The equilibrium solution with a certain value of Φ_z is calculated as follows: first slowly adjust Φ_z to the target value and then let the system relax to the equilibrium state, during which Φ_z is maintained to be conserved at the target value, which is achieved by the same numerical measure as that introduced in Hu et al. (2003).

3. Simulation Results

3.1. Force-free Condition

We analyze the evolution of the magnetic system under force-free conditions, and the evolution of the system is purely determined by magnetic forces. As mentioned in Section 2, different values of (a, b, c, d, σ) correspond to different background fields, resulting in different magnetic systems. Here we adjust the distance between the inner pair of the charges, $d_s = 2a$, and their strength, which is characterized by the value of σ, to obtain magnetic systems with different photospheric flux distributions. The width of these charges is always fixed at $w = b - a = d - c = 20$ Mm, and the distance between the inner and the outer pair of charges is also fixed at $D = c - b = 5$ Mm.

The initial configurations with $d_s = 0.0$, 2.0, 4.0, 6.0, 8.0, 10.0 Mm are shown in Figures 2(a)–(c) and (g)–(i), respectively, with the same $\sigma = 1.0$. The photospheric distribution of the corresponding normal component of the magnetic field, B_y, is plotted in Figures 2(d)–(f) and (j)–(l). B_y corresponds to the radial component of the photospheric magnetic fields in observations. For each flux rope system, starting from the initial state we increase the axial magnetic flux Φ_z to calculate different equilibrium solutions, as shown by the red dots in Figure 3. The poloidal flux Φ_p of the rope for all equilibrium

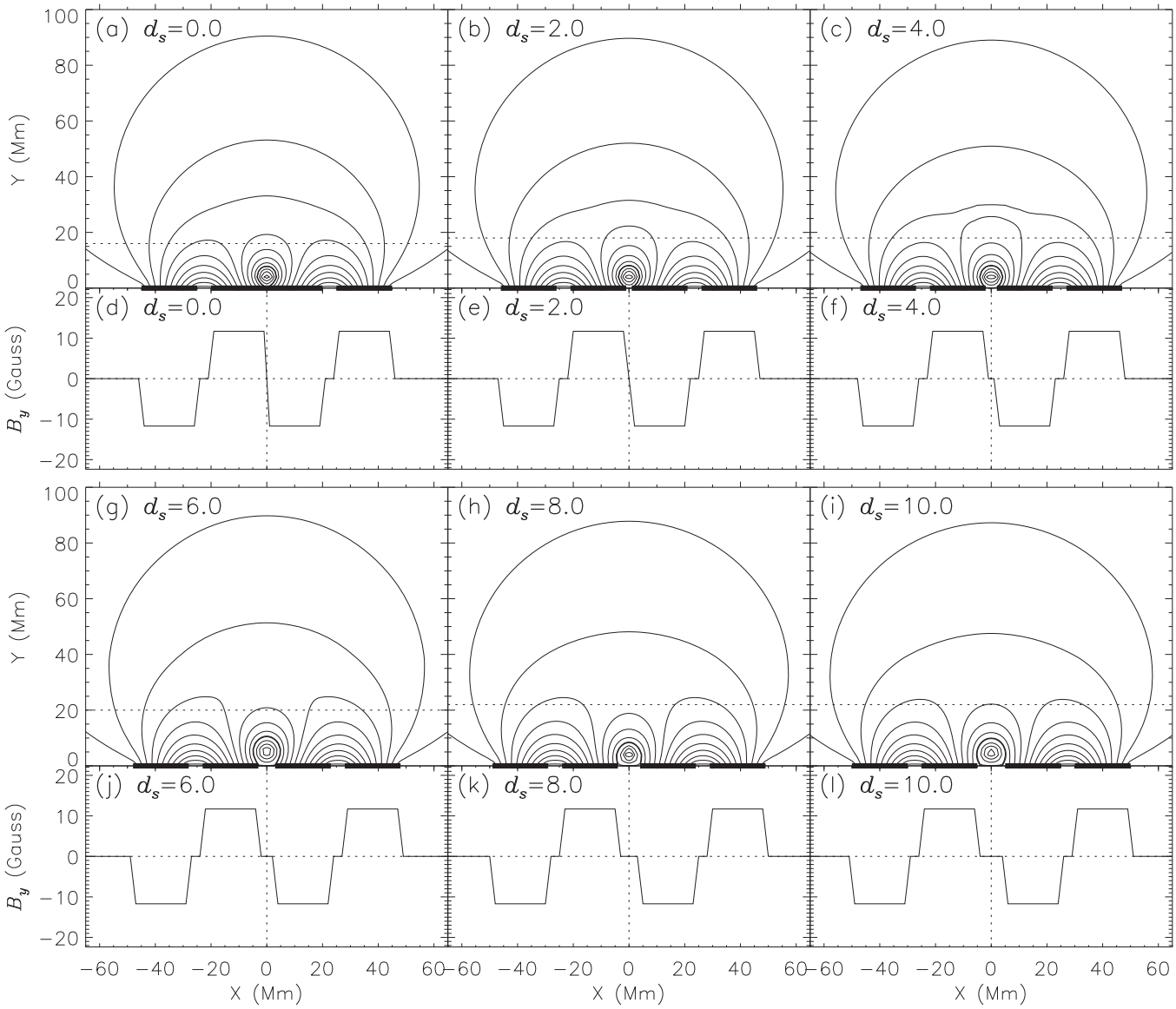

Figure 2. Initial configurations and the corresponding normal components of the magnetic field (B_y) at the photosphere ($y = 0$) for a different d_s, which is selected to be 0.0, 2.0, 4.0, 6.0, 8.0, 10.0 Mm, respectively; σ is 1.0 for all six cases. The two pairs of surface magnetic charges for different cases are marked by the black solid lines at $y = 0$ in panels (a)–(c) and (g)–(i). The height of the neutral point in the quadrupolar background field is marked by the horizontal dotted line in panels (a)–(c) and (g)–(i).

solutions in Figure 3 is fixed at $\Phi_p^0 = -7.5 \times 10^9\,\mathrm{Mx\,cm^{-1}}$. Figures 3(a)–(c) and (g)–(i) plot the evolutions of H, and Figure 3(d)–(f) and (j)–(l) plot those of L_c. With an increasing Φ_z, the flux rope evolves from the sticky state to the levitating state. As shown in Figure 3, the transition between these two kinds of states is quite different for different values of d_s. For the cases with a small enough d_s, i.e., $d_s = 0.0$ and 2.0 Mm, the transition from the sticky state to the levitating state is continuous, indicating that these magnetic systems are noncatastrophic, whereas for $d_s \geqslant 4.0$ Mm, the sticky and levitating equilibrium states are diverged into upper and lower branches, respectively, and the transition is manifested as a discontinuous jump from the lower branch to the upper branch; i.e., this is an upward catastrophe. Note that for the noncatastrophic cases H and L_c will saturate for a further increasing Φ_z, so that these flux rope systems should be non-eruptive. The upward catastrophic points are marked by the red vertical dotted lines in Figure 3. An example of the upward catastrophe is exhibited in Figures 4(a) and (b), which illustrate the equilibrium states of the systems with $d_s = 10.0$ Mm just before and after the upward catastrophe. The flux rope keeps sticking to the photosphere until the upward catastrophic point $\Phi_z^u = 17.2 \times 10^{18}$ Mx, across which the flux rope quickly jumps upward and levitates in the corona. The transition from the BPSS configuration to the HFT configuration with increasing axial flux has also been shown by studies based on NLFFF extrapolations (Savcheva & van Ballegooijen 2009; Su et al. 2011; Savcheva et al. 2015). The simulation results reveal that under force-free conditions, if the surface charges are not too close, then an upward catastrophe could also exist in the quadrupolar background field.

In the simulations discussed above (as shown by the red dots), we have obtained equilibrium states with the flux rope levitating in the corona for magnetic systems with different photospheric flux distributions. Starting from these levitating states, we decrease the control parameter (Φ_z) to calculate new

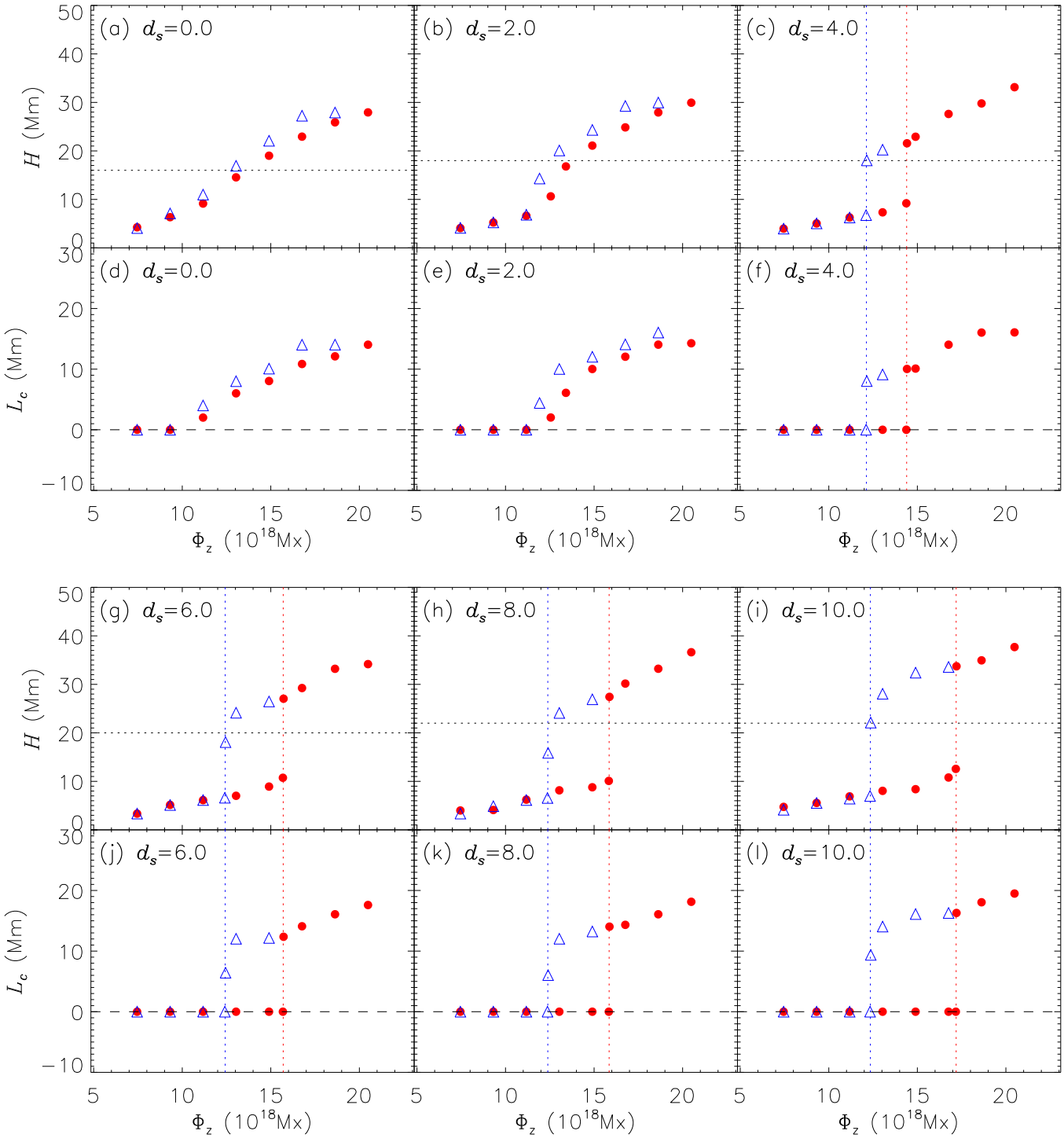

Figure 3. Height of the flux rope axis (H) and the length of the current sheet below the rope (L_c) are shown as functions of the control parameter (Φ_z) for quadrupolar background fields with a different d_s under force-free conditions. The red points represent the transition from sticky states to levitating states and the blue triangles represent the transition from levitating states to sticky states. The vertical dotted lines represent the catastrophic points of the catastrophic cases. The height of the neutral point in the quadrupolar background field is marked by the horizontal dotted line in panels (a)–(c) and (g)–(i).

equilibrium states so as to investigate the transition from the levitating state to the sticky state following a route distinctive from the former transition. As shown by the blue triangles in Figure 3, the type of this transition also varies with photospheric flux distributions. For the systems that have an upward catastrophe, i.e., $d_s \geqslant 4.0$ Mm, there also exists a downward catastrophe from the upper branch to the lower branch; the downward catastrophic points are marked by the blue dotted lines in Figure 3. These cases are similar to that simulated in Zhang et al. (2016). The equilibrium solutions of the systems with $d_s = 10.0$ Mm just before and after the downward catastrophe are also illustrated in Figures 4(c) and (d); the downward catastrophic point is $\Phi_z^d = 12.3 \times 10^{18}$ Mx. For the systems with $d_s = 0.0$ and 2.0 Mm, however, the transition from the levitating states to the sticky states is still continuous, indicating that there is no downward catastrophe either. Thus

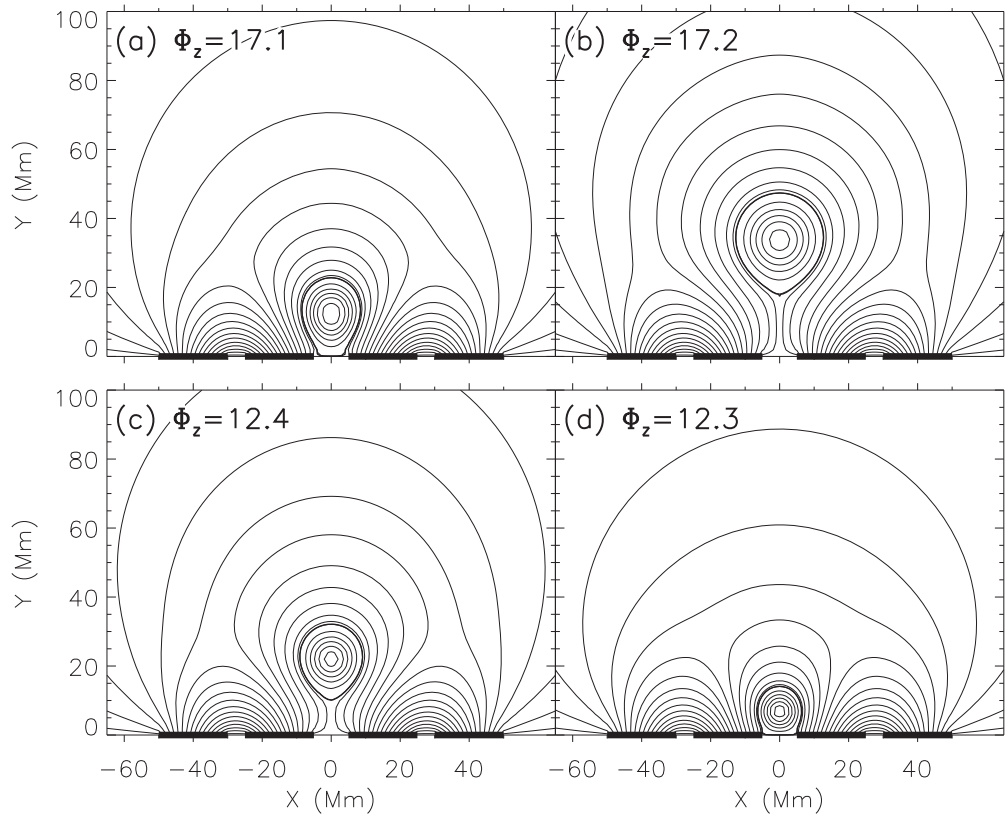

Figure 4. Magnetic configurations of the flux rope system (a) right before and (b) after the upward catastrophe and (c) right before and (d) after the downward catastrophe for the case with $d_s = 10.0$ Mm and $\sigma = 1.0$.

we may conclude that a downward catastrophe also exists in the quadrupolar background field under force-free conditions and that the equilibrium states of the system are diverged into upper and lower branches by the upward and downward catastrophes when the photospheric flux is not concentrated too much toward the PIL; otherwise the transition between the sticky and levitating states is continuous so that neither upward nor downward catastrophe occurs.

Photospheric flux distribution also influences the properties of upward and downward catastrophes, as tabulated in Table 1. The upward catastrophic point Φ_z^u increases with an increasing d_s, which implies that the background field with a larger d_s exerts a stronger constraint on the flux rope. The amplitude of the upward catastrophe L_z^u also increases with an increasing d_s, indicating that the upward catastrophe is more drastic in the system with a larger d_s; i.e., the system with a larger d_s tends to produce larger activities. The downward catastrophic point Φ_z^d is almost the same in catastrophic systems with a different d_s, from which we may infer that the influence of d_s on a downward catastrophe may be somewhat different from its influence on an upward catastrophe. This may be the reason why the variation of the downward catastrophic amplitude L_z^d with d_s is also slightly different from that of L_z^u. Moreover, as seen from Table 1, the separation between the two catastrophic points, $\Phi_z^u - \Phi_z^d$, also increases with an increasing d_s. This indicates that with an increasing d_s the system first evolves from a noncatastrophic one to a catastrophic one, and then the two catastrophes are increasingly separated.

Apart from d_s, we also adjust σ by adjusting the charge density of the inner pair of surface charges (with a fixed d_s) to obtain different photospheric flux distributions. The initial

Table 1
Parameters of the Catastrophes vs. d_s for $\sigma = 1.0$

d_s(Mm)	Φ_z^u(10^{10} Wb)	L_c^u(Mm)	Φ_z^d(10^{10} Wb)	L_c^d(Mm)	$\Phi_z^u - \Phi_z^d$(10^{10} Wb)
4.0	14.4	10.0	12.1	8.0	2.3
6.0	15.7	12.4	12.4	6.0	3.3
8.0	15.9	14.0	12.4	6.0	3.5
10.0	17.2	16.3	12.3	9.4	4.9

Note. Φ_z^u and Φ_z^d represent the upward and downward catastrophic points, respectively; L_c^u and L_c^d are the spatial amplitudes of the upward and downward catastrophes, respectively.

configurations with $\sigma = 0.6$, 0.8, 1.0, 1.2, 1.4, 1.6 are shown in Figures 5(a)–(c) and (g)–(i), respectively, with the same $d_s = 10.0$ Mm. The corresponding B_y is plotted in Figures 5(d)–(f) and (j)–(l). A smaller σ implies a weaker inner pair of charges, corresponding to less magnetic flux of the background field above the flux rope so that the constraint exerted by the background field on the flux rope is also weaker. Following similar simulating procedures as those introduced above, the evolution of the flux rope in systems with a different σ as a function of Φ_z are calculated, as shown in Figure 6. The poloidal flux Φ_p of the rope is fixed at -3.7×10^9 Mx cm^{-1} for the case with $\sigma = 0.6$ and at -7.5×10^9 Mx cm^{-1} for the other cases. For $\sigma = 0.6$, the transition between the sticky state and the levitating state is always continuous, i.e., neither upward nor downward catastrophe exists in this system. Thus we may conclude that if the constraint of the background field on the flux rope is too weak, then the system should be noncatastrophic. For

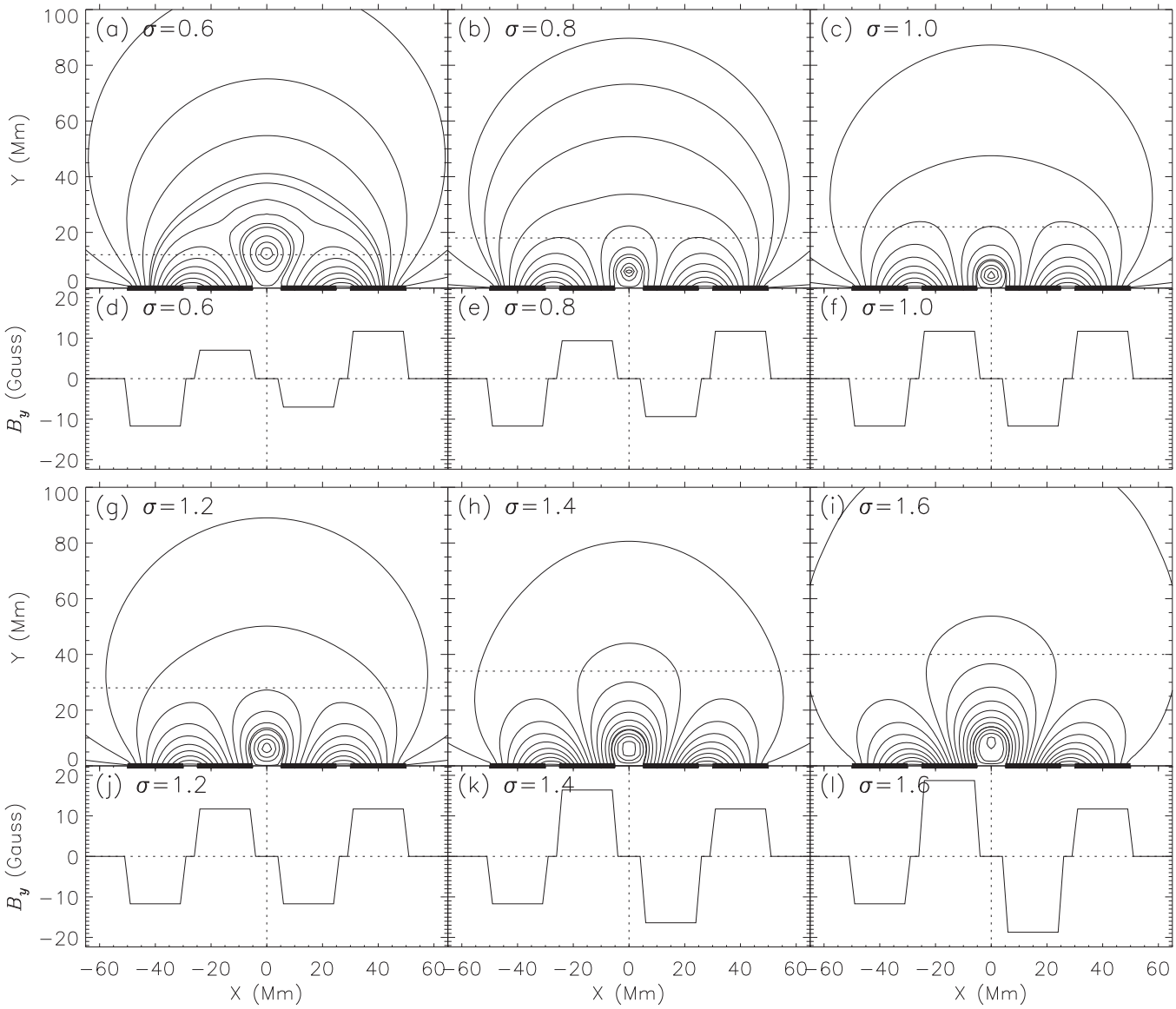

Figure 5. Quadrupolar background configurations and the corresponding normal components of the magnetic field (B_y) at the photosphere ($y = 0$) for a different σ, which is selected to be 0.6, 0.8, 1.0, 1.2, 1.4, 1.6 Mm, respectively; d_s is 10.0 Mm for all the six cases. The two pairs of surface magnetic charges for different cases are marked by the black solid lines at $y = 0$ in panels (a)–(c) and (g)–(i). The height of the neutral point in the quadrupolar background field is marked by the horizontal dotted line in panels (a)–(c) and (g)–(i).

$\sigma \geqslant 0.8$, the equilibrium states of these systems are diverged into upward and downward branches, which are only connected by the upward and downward catastrophes. The properties of the catastrophes in magnetic systems with a different σ are tabulated in Table 2. The catastrophic points of both the upward and downward catastrophes increase with an increasing σ, as do the amplitudes of the catastrophes. This indicates that both the upward and downward catastrophes in the system with a larger σ are more drastic, so that the magnetic system with a larger σ tends to produce larger active region activities. The difference $\Phi_z^u - \Phi_z^d$ also increases with an increasing σ, similar to that with d_s.

In summary, under the force-free condition the catastrophic behaviors of the magnetic system consisting of a flux rope in a fully closed quadrupolar background field are influenced by the photospheric magnetic conditions. The system could have both an upward and a downward catastrophe, provided that the photospheric flux distribution is not concentrated too much toward the PIL and the constraint exerted by the background field on the flux rope is not too weak. A downward catastrophe is always accompanied by an upward catastrophe so that the equilibrium states of the system are diverged into two branches by these two catastrophes. With an increasing d_s and σ, the flux rope activities in the system tends to be stronger.

3.2. Non-force-free Condition

The flux rope system does not always satisfy force-free approximation. For example, prominences are cool and dense plasma is suspended in the hot and diluted corona (e.g., Wang et al. 2010; Liu et al. 2012a, 2012b), so that a flux rope system containing a prominence should be far from force free. To be comprehensive in our investigation of the evolution of a flux rope in a quadrupolar background field, we also simulate the evolution of the flux rope system under the non-force-free

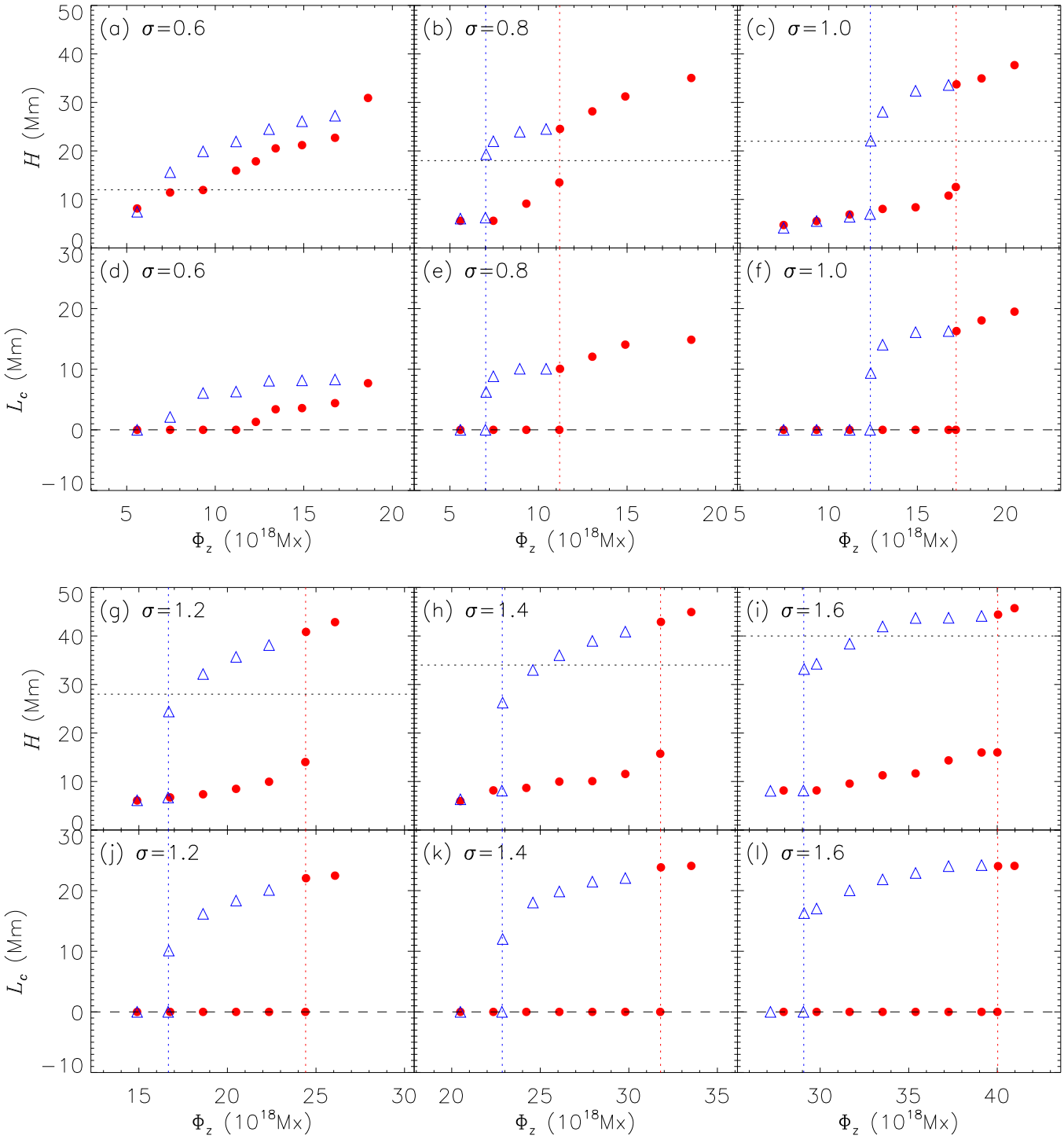

Figure 6. H and L_c vs. Φ_z for quadrupolar background fields with a different σ under force-free conditions. The meanings of the symbols are the same as those in Figure 3.

condition. Here we calculate two cases: $d_s = 0.0$ Mm, $\sigma = 1.0$ and $d_s = 10.0$ Mm, $\sigma = 1.0$. Under the non-force-free condition, the flux rope is characterized by not only the magnetic parameters, Φ_z and Φ_p, but also M, the mass of the rope per unit length, which is always fixed at $M = 334$ g cm^{-1} in the simulation. Assuming that the length of the flux rope is about 100 Mm, the mass of the flux rope would be 3.3×10^{12} g, which is comparable to the lower values of the observed mass range of solar prominences (Labrosse et al. 2010; Parenti 2014).

Removing the relaxation procedure introduced in Section 2, the magnetostatic equilibrium solutions with different Φ_z but the same $\Phi_p = -3.7 \times 10^9$ Mx cm^{-1} are calculated. As shown in Figure 7, when d_s is large enough there are also upward and downward catastrophes in the quadrupolar field under non-force-free conditions; otherwise the geometric parameters vary continuously with an increasing or decreasing Φ_z. Thus we may conclude that upward and downward catastrophe also exist in the quadrupolar field under non-force-free conditions and the

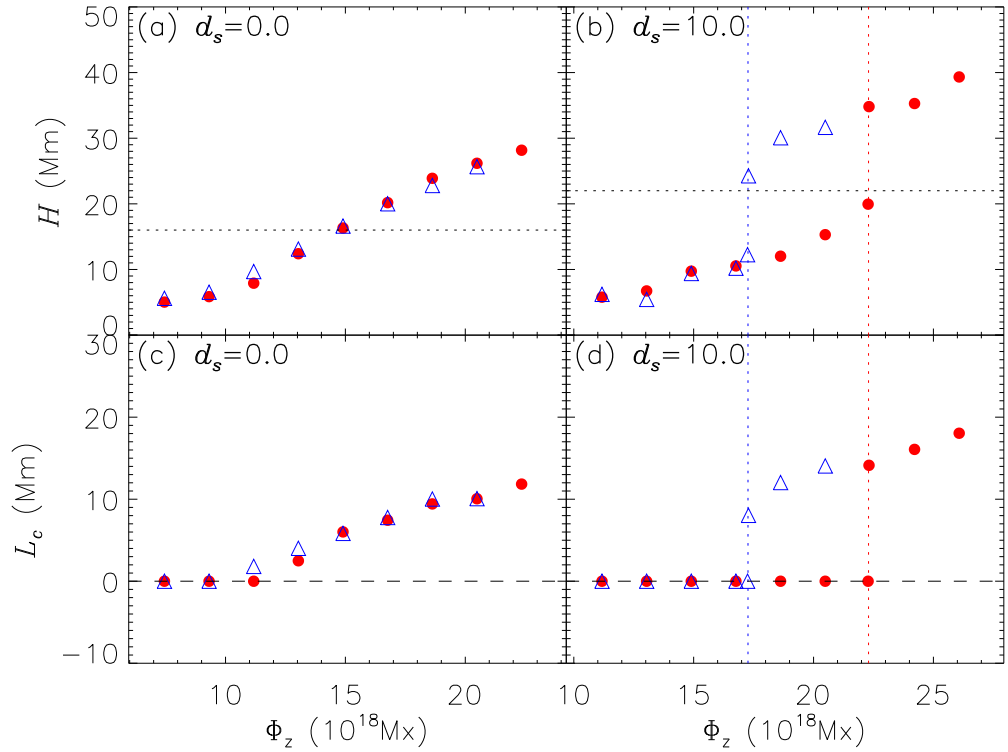

Figure 7. H and L_c vs. Φ_z for quadrupolar background fields with a different σ under non-force-free conditions. The meanings of the symbols are the same as those in Figure 3.

Table 2
Parameters of the Catastrophes vs. σ for d_s = 10.0 Mm

σ	Φ_z^u(10^{10} Wb)	L_c^u(Mm)	Φ_z^d(10^{10} Wb)	L_c^d(Mm)	$\Phi_z^u - \Phi_z^d$(10^{10} Wb)
0.8	11.2	10.1	7.0	6.3	4.2
1.0	17.2	16.3	12.3	9.4	4.9
1.2	24.4	22.0	16.6	10.1	7.8
1.4	31.8	23.8	22.8	12.0	9.0
1.6	40.0	24.0	29.0	16.3	11.0

Note. The meanings of the parameters are the same as those in Table 1.

existence of the catastrophes is influenced by the photospheric magnetic conditions, which are similar to the conclusions reached above under force-free conditions.

4. Upward Catastrophe versus Torus Instability

The equilibrium of a coronal magnetic flux rope is usually simplified as the balance between the upward Lorentz force resulting from the oppositely directed image current of the flux rope (also called hoop force in some papers) and the downward Lorentz force from the constraint of the external poloidal magnetic field (Kliem et al. 2014). By analyzing these two Lorentz forces acting on the flux rope, it is found that if the external magnetic field of a flux rope system, $B_{\rm ex}$, decreases fast enough with the height above the photosphere, then the flux rope is unstable to an upward disturbance, which is called torus instability (Kliem & Török 2006; Zuccarello et al. 2016). The decrease of the external field is described by the decay index $n = -d(\ln B_{ex})/d(\ln h)$. Based on the wire current model, it is derived that torus instability occurs if n is larger than 1 for straight-current channels (Van Tend & Kuperus 1978; Filippov & Den 2001) and larger than 1.5 for circular cases (Kliem & Török 2006). Both theoretical and observational studies found that torus instability plays an important role in triggering flux rope eruptions (e.g., Török & Kliem 2007; Guo et al. 2010).

Catastrophes have a close relationship with instabilities. By setting the analysis of loss of equilibrium and stability analysis in the same analytical framework, Démoulin & Aulanier (2010) suggested that upward catastrophe and torus instability should be two different views of the same physical mechanism. Furthermore, Kliem et al. (2014) made a comprehensive analytical study about the relationship between torus instability and upward catastrophe triggered by variations of the photospheric flux distributions and found that the nose point of the equilibrium manifold, at which the upward catastrophe occurs, just connects the stable and unstable branches of the equilibrium states. In other words, at this nose point, not only does upward catastrophe occur, but the system also evolves from a stable equilibrium to an unstable equilibrium, so that torus instability occurs as well. Therefore Kliem et al. (2014) concluded that upward catastrophe and torus instability should be equivalent descriptions for the onset condition of solar eruptions.

In this paper, we have simulated the evolution of the flux rope system versus the variation of the flux rope itself under different photospheric magnetic conditions. In order to investigate the role that torus instability plays in our simulation, we calculate the decay index of the external magnetic field under different photospheric magnetic conditions. Here the external magnetic field is just the background field for each case, which is a potential quadrupolar field. Note that the flux rope model in our simulation is different from that for torus instability in many aspects, so the analysis here is only semiquantitative. Figure 8(a) illustrates the variations of the

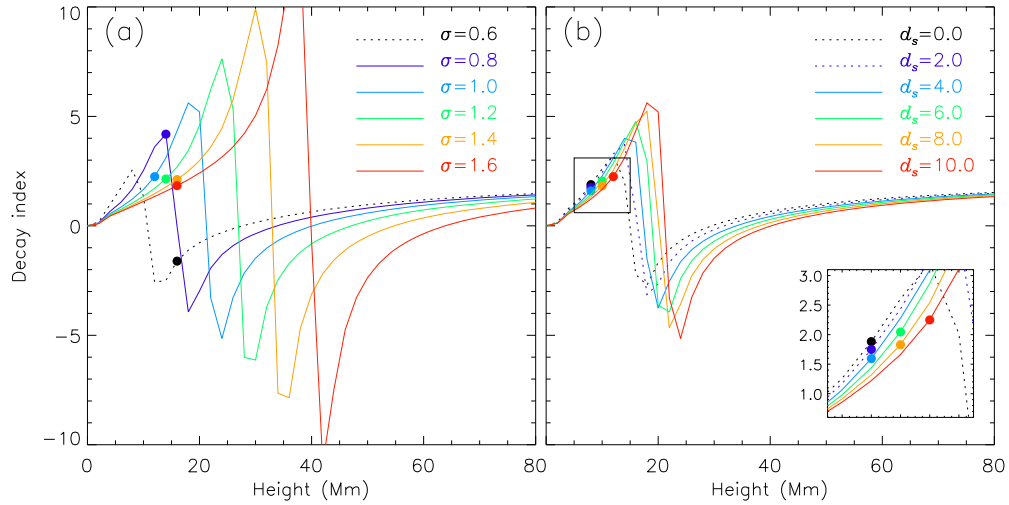

Figure 8. Decay indices of the external field in different flux rope systems. Panel (a) shows the variations of the decay index with the height along $x = 0$ for a different σ, and panel (b) shows those for a different d_s; the catastrophic cases are plotted in solid lines, and the noncatastrophic ones are shown in dotted lines.

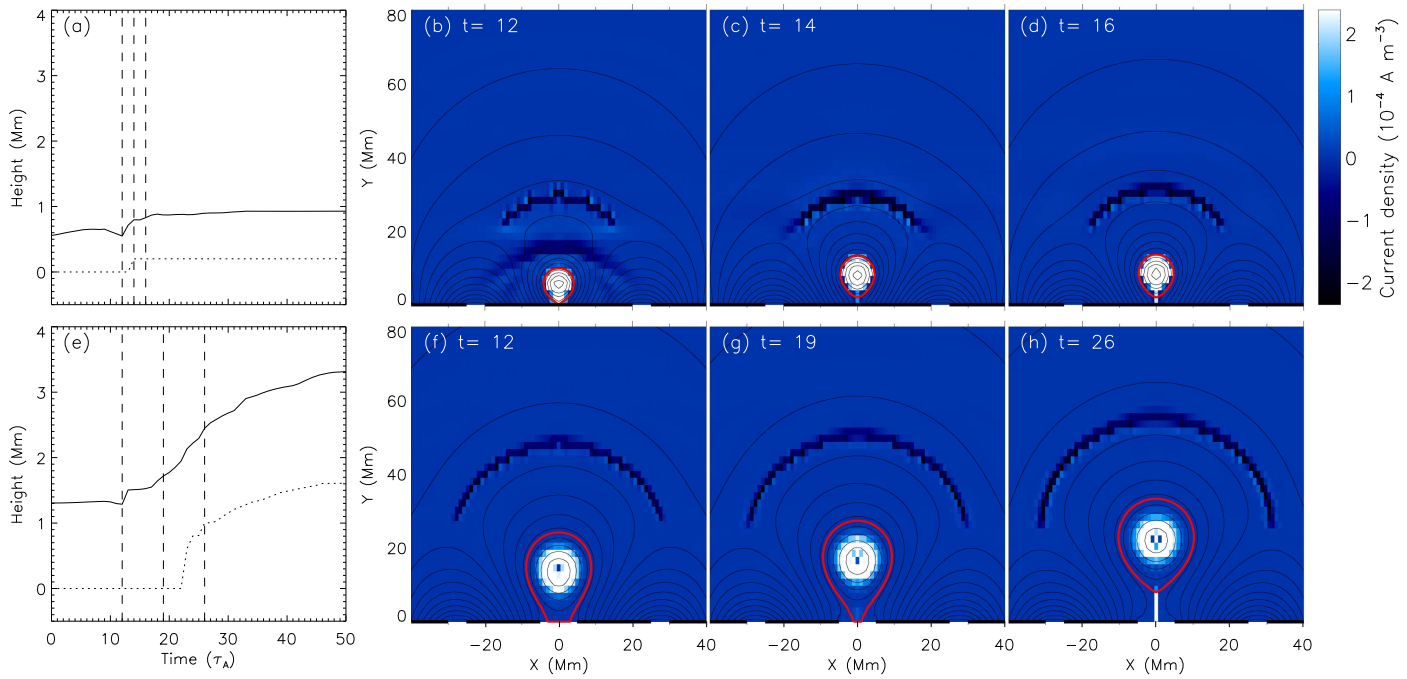

Figure 9. Dynamic processes during which the flux rope breaks away from the photosphere in noncatastrophe (top panels) and catastrophe (bottom panels). Panel (a) plots the variations of the height of the rope axis (solid lines) and the length of the current sheet below the flux rope (dotted lines) in the system with $d_s = 0.0$ Mm. The distributions of j_z at different times are illustrated in panels (b)–(d), as marked by the vertical dashed lines in panel (a), respectively. Panel (e) plots the variations of geometric parameters in the system with $d_s = 10.0$ Mm, and the corresponding distributions of j_z are illustrated in panels (f)–(h). The boundaries of the flux rope are marked by the red curves.

decay index along $x = 0$ for a different σ. The noncatastrophic cases are plotted in dotted lines and the catastrophic ones in solid lines. The dots represent the location of the rope axis in the equilibrium state right before the flux rope breaks away from the photosphere. It should be noted that our simulation is 2.5-dimensional, indicating that what we analyze here is the torus instability of a straight flux rope in the quadrupolar field. As shown by Figure 8(a), the decay indices at the rope axis for the catastrophic cases are at least 1.8, so the flux rope is probably torus unstable in these catastrophic cases. For the noncatastrophic case with $\sigma = 0.6$, however, the decay index at the rope axis is only -1.6, indicating a torus-stable system. Therefore, for different flux rope systems with a different σ, upward catastrophe is in good correspondence with torus instability.

The variations of the decay index along $x = 0$ for a different d_s are shown in Figure 8(b). Similarly, the catastrophic and noncatastrophic cases are plotted in solid and dotted lines, respectively. Different from σ, all the flux rope systems with a different d_s have decay indices of no less than 1.59, i.e., all these flux rope systems are probably torus unstable. This indicates that torus-unstable systems could also be noncatastrophic. To find out the cause, we compare the dynamic processes during which the flux rope breaks away from the photosphere in noncatastrophic and catastrophic cases, as shown in Figure 9. Figure 9(a) is the calculation for the

equilibrium state with $\Phi_z = 11.4 \times 10^{18}$ Mx in the system with $d_s = 0.0$ Mm, i.e., the state right after the flux rope breaks away from the photosphere. The variations of the height of the rope axis and the length of the current sheet below the flux rope are plotted by solid and dotted lines, respectively. The unit of time is $\tau_A = 17.4$ s. Figures 9(b)–(d) are the distributions of the current in $z-$ direction, j_z, at different times, as marked by vertical dashed lines in Figure 9(a); the boundary of the flux rope is marked by the red curves. At first the flux rope sticks to the photosphere; then Φ_z adjusts to 11.4×10^{18} Mx and the system relaxes to the equilibrium state. At the time $t = 12\ \tau_A$, the flux rope begins to break away from the photosphere (Figure 9(b)), which is almost immediately followed by the appearance of the current sheet below the flux rope at $t = 14\ \tau_A$ (Figure 9(c)). Since the net current within the flux rope and the current sheet below the flux rope have the same direction, a downward force is exerted by the newly formed current sheet on the flux rope so that the upward motion of the flux rope is also immediately terminated (Figure 9(d)), resulting in a continuous transition from the sticky state to the levitating state. Although the decay index is rather large (here $n = 1.9$), torus instability should be prohibited by the quickly generated current sheet below the flux rope at the very beginning (B. Kliem 2017, private communication). Then the force balance of the flux rope is determined not only by the hoop force and the Lorentz force of the external field, but also by the drag force from the current sheet below the rope. If Φ_z is larger, then a stronger drag force is also needed so that the flux rope levitates at a higher height with a longer current sheet beneath. Therefore, in the system with $d_s = 0.0$ Mm, the H and L_c increase continuously with the control parameter Φ_z so that the system is noncatastrophic. The system with $d_s = 0.1$ Mm also has a similar conclusion. Figure 9(e) is the calculation for the equilibrium state with $\Phi_z = 17.2 \times 10^{18}$ Mx in the system with $d_s = 10.0$ Mm, i.e., the state right after upward catastrophe occurs; Figures 9(f)–(h) is the corresponding distributions of j_z. Different from that in Figure 9(a), although the flux rope also begins to break away from the photosphere at $t = 12\ \tau_A$, the current sheet below the flux rope does not appears until $t = 22\ \tau_A$, as shown in Figure 9(g). During this period, the underside of the flux rope keeps sticking to the photosphere (see Figure 9(g)), which is somewhat similar to the line-tied effect (e.g., Isenberg & Forbes 2007; Aulanier et al. 2010). Since there is no current sheet below the flux rope during this period and a torus-unstable condition should be satisfied (here $n = 2.2$), torus instability occurs so that the flux rope keeps rising. After $t = 22\ \tau_A$, the flux rope detaches from the photosphere (see Figure 9(h)) and the current sheet appears below the flux rope, which prevents the further evolution of torus instability. Eventually, the flux rope levitates at a certain height, resulting in a equilibrium state discontinuous from the state with $\Phi_z < 17.2 \times 10^{18}$ Mx, whose L_c is always 0. Therefore there is an upward catastrophe in the system with $d_s = 10.0$ Mm. The major difference in this system from that with $d_s = 0.0$ Mm is the obvious delay of the appearance of the current sheet, during which torus instability could evolve to a certain extent so that upward catastrophe could occur in this system.

In summary, we may infer that torus unstable may be a necessary but not sufficient condition for upward catastrophe; torus-unstable systems could also be noncatastrophic. This is because the analysis for torus instability does not take the effect of the current sheet below the flux rope into account. Our simulation results demonstrate that the current sheet below the flux rope is also important for the onset condition of solar eruption: if the current sheet appears immediately after the flux rope moves upward, then torus instability will be prohibited at the very beginning so that the system is noncatastrophic, and as a result there is no eruption in this system. As we have discussed, the appearance time of the current sheet is significantly influenced by photospheric flux distributions.

5. Discussion and Conclusion

To investigate the catastrophic behavior of flux rope systems in strong active regions, we simulate the evolution of the magnetic system consisting of a flux rope in fully closed quadrupolar background fields with different photospheric flux distributions. Under a force-free condition, it is found that when the photospheric flux is not concentrated too much toward the PIL (a large-enough d_s) and the constraint exerted by the background field is not too weak (a large-enough σ), the equilibrium states of the system are separated into two branches that are connected by an upward and a downward catastrophe, respectively. Otherwise, the geometric parameters always evolve continuously with a varying Φ_z. Therefore we may conclude that the downward catastrophe also exists in quadrupolar fields, and the upward and downward catastrophes are always paired with each other. Moreover, the properties of both the upward and the downward catastrophes are also influenced by the photospheric flux distribution; a larger d_s and σ not only favor the existence of the catastrophes but also result in a more drastic evolutionary profile when there exist catastrophes; i.e., a system with a larger d_s and σ tends to produce stronger active region activities. A similar conclusion also holds for the magnetic system under a non-force-free condition. The magnetic configuration in our simulation is similar to that in the breakout scenario, in which the eruption is triggered by the reconnection at the upper current sheet. By simulations in the bipolar field, Zhang et al. (2017) found that catastrophe only exists when the photospheric flux is concentrated not too much toward the central region and the background field is not too weak, which is consistent with our simulation results in the quadrupolar field.

For the flux rope systems with different photospheric magnetic conditions, we also calculate the decay index at the rope axis in the state right before the flux rope leaves the photosphere. It is revealed that upward catastrophe and torus instability should have a close relationship: catastrophic flux rope systems tend to be torus unstable, whereas torus-unstable systems may not always be catastrophic; the current sheet below the flux rope may also be important for the onset of flux rope eruptions. In our simulation the flux rope has a finite cross-section, so that the critical decay index derived based on the wire current model, 1 for the straight current channel and 1.5 for the circular current channel, can hardly be directly used in the analysis for our simulation results, so the analysis here is only semiquantitative. Since a downward catastrophe is always paired with an upward catastrophe in our simulation, we may infer that the non-eruptive downward catastrophe also tends to occur in a magnetic system with strong decay in the magnetic fields above the flux rope.

By using a simplied analytic flux rope model in quadrupolar magnetic fields, Longcope & Forbes (2014) analyzed the quasi-static evolution with the changes at the boundary or the

reconnection above and under the flux rope and found that all three kinds of evolutionary scenarios can lead to catastrophe. In our simulations, it is demonstrated that the processes resulting in the changes of the flux rope properties can also trigger catastrophes, and both the existence and the properties of the catastrophes are influenced by the photospheric magnetic conditions. The analytical study in Longcope & Forbes (2014) and our simulations reveal different aspects of the catastrophes in quadrupolar magnetic fields.

We are grateful to Dr. Bernhard Kliem for his guidance and suggestions in the analysis about the relationship between catastrophe and torus instability. We also appreciate the anonymous referee for valuable comments that significantly improved this paper. This research is supported by NSFC grants 41131065, 41574165, 41421063, 41474151 and 41222031; MOEC grant 20113402110001; the CAS Key Research Program KZZD-EW-01-4; and the fundamental research funds for the central universities, WK2080000077. R.L. acknowledges the support from the Thousand Young Talents Program of China.

ORCID iDs

Quanhao Zhang https://orcid.org/0000-0003-0565-3206
Yuming Wang https://orcid.org/0000-0002-8887-3919
Rui Liu https://orcid.org/0000-0003-4618-4979
Kai Liu https://orcid.org/0000-0003-2573-1531
Jiajia Liu https://orcid.org/0000-0003-2569-1840

References

Amari, T., Luciani, J. F., Mikic, Z., & Linker, J. 2000, ApJL, 529, L49
Antiochos, S. K., DeVore, C. R., & Klimchuk, J. A. 1999, ApJ, 510, 485
Aulanier, G., Török, T., Démoulin, P., & DeLuca, E. E. 2010, ApJ, 708, 314
Chen, P. F. 2011, LRSP, 8, 1
Chen, P. F., & Shibata, K. 2000, ApJ, 545, 524
Chen, Y., Hu, Y. Q., & Sun, S. J. 2007a, ApJ, 665, 1421
Chen, Y., Hu, Y. Q., & Xia, L. D. 2007b, AdSpR, 40, 1780
Démoulin, P., & Aulanier, G. 2010, ApJ, 718, 1388
Filippov, B. P., & Den, O. G. 2001, JGR, 106, 25177
Forbes, T. G. 1990, JGR, 95, 11919
Forbes, T. G., & Isenberg, P. A. 1991, ApJ, 373, 294
Forbes, T. G., & Priest, E. R. 1995, ApJ, 446, 377
Green, L. M., & Kliem, B. 2009, ApJL, 700, L83
Green, L. M., Kliem, B., & Wallace, A. J. 2011, A&A, 526, A2
Guo, Y., Ding, M. D., Schmieder, B., et al. 2010, ApJL, 725, L38
Hu, Y. Q. 1989, JCoPh, 84, 441
Hu, Y. Q. 2001, SoPh, 200, 115
Hu, Y. Q. 2004, ApJ, 607, 1032
Hu, Y. Q., Li, G. Q., & Xing, X. Y. 2003, JGRA, 108, 1072
Hu, Y. Q., & Liu, W. 2000, ApJ, 540, 1119
Isenberg, P. A., & Forbes, T. G. 2007, ApJ, 670, 1453
Isenberg, P. A., Forbes, T. G., & Demoulin, P. 1993, ApJ, 417, 368
Janvier, M., Savcheva, A., Pariat, E., et al. 2016, A&A, 591, A141
Kliem, B., Lin, J., Forbes, T. G., Priest, E. R., & Török, T. 2014, ApJ, 789, 46
Kliem, B., & Török, T. 2006, PhRvL, 96, 255002
Labrosse, N., Heinzel, P., Vial, J.-C., et al. 2010, SSRv, 151, 243
Lin, J., & Forbes, T. G. 2000, JGRA, 105, 2375
Lin, J., & van Ballegooijen, A. A. 2002, ApJ, 576, 485
Liu, K., Wang, Y., Shen, C., & Wang, S. 2012a, ApJ, 744, 168
Liu, R., Alexander, D., & Gilbert, H. R. 2007, ApJ, 661, 1260
Liu, R., Kliem, B., Török, T., et al. 2012b, ApJ, 756, 59
Longcope, D. W., & Forbes, T. G. 2014, SoPh, 289, 2091
Low, B. C. 1996, SoPh, 167, 217
Moore, R. L., Sterling, A. C., Hudson, H. S., & Lemen, J. R. 2001, ApJ, 552, 833
Parenti, S. 2014, LRSP, 11, 1
Priest, E. R., & Forbes, T. G. 1990, SoPh, 126, 319
Savcheva, A., Pariat, E., McKillop, S., et al. 2015, ApJ, 810, 96
Savcheva, A., Pariat, E., McKillop, S., et al. 2016, ApJ, 817, 43
Savcheva, A., & van Ballegooijen, A. 2009, ApJ, 703, 1766
Schrijver, C. J., Aulanier, G., Title, A. M., Pariat, E., & Delannée, C. 2011, ApJ, 738, 167
Shibata, K., & Magara, T. 2011, LRSP, 8, 6
Su, Y., Surges, V., van Ballegooijen, A., DeLuca, E., & Golub, L. 2011, ApJ, 734, 53
Sun, X., Hoeksema, J. T., Liu, Y., et al. 2012, ApJ, 748, 77
Titov, V. S., & Démoulin, P. 1999, A&A, 351, 707
Titov, V. S., Hornig, G., & Démoulin, P. 2002, JGRA, 107, 1164
Titov, V. S., Priest, E. R., & Demoulin, P. 1993, A&A, 276, 564
Török, T., & Kliem, B. 2007, AN, 328, 743
van Driel-Gesztelyi, L., & Green, L. M. 2015, LRSP, 12, 1
Van Tend, W., & Kuperus, M. 1978, SoPh, 59, 115
Wang, Y., Cao, H., Chen, J., et al. 2010, ApJ, 717, 973
Wang, Y., Zhou, Z., Shen, C., Liu, R., & Wang, S. 2015, JGRA, 120, 1543
Zhang, Q., Wang, Y., Hu, Y., & Liu, R. 2016, ApJ, 825, 109
Zhang, Q., Wang, Y., Hu, Y., Liu, R., & Liu, J. 2017, ApJ, 835, 211
Zhang, Y.-Z., & Wang, J.-X. 2007, ApJ, 663, 592
Zhao, J., Li, H., Pariat, E., et al. 2014, ApJ, 787, 88
Zuccarello, F. P., Aulanier, G., & Gilchrist, S. A. 2016, ApJL, 821, L23